Drag coefficient and flow structure downstream of mangrove root-type models through PIV and direct force measurements

Amirkhosro Kazemi,[1] Keith Van de Riet,[2] and Oscar M. Curet[1,*]
[1]*Department of Ocean and Mechanical Engineering, Florida Atlantic University, Boca Raton, Florida 33431, USA*
[2]*School of Architecture and Design, University of Kansas, Lawrence, Kansas 66045, USA*

(Received 23 August 2017; published 18 July 2018)

Mangrove trees form dense networks of prop roots in coastal intertidal zones. The interaction of mangroves with tidal and river flows is fundamental to the preservation of estuaries and shorelines by providing water filtration, protection against erosion, and habitat for aquatic animals. The impact of mangrove roots on unidirectional flows is mainly characterized by hydrodynamics including drag, flow structures, transport, and fluid-structure interaction. In this work, we focus on the drag coefficient and flow structure downstream of simplified mangrove root models. The mangrove roots were modeled as a cluster of uniformly distributed rigid circular cylinders (patch), with a frontal area per unit volume (a). Direct force measurements were made in a recirculating water flume. In addition, the unsteady wake was measured using particle image velocimetry (PIV). The models were tested for a Reynolds number range of 600 to 12 000 based on the patch diameter ($\mathrm{Re}_D = \frac{\rho U D}{\mu}$), in order to resemble natural conditions. A new length scale, the "effective diameter," is proposed by comparing the Strouhal number of the patches with the analytical Strouhal number of a canonical cylinder in the flow field that produces the same vortex shedding. We compared different length scales to characterize the hydrodynamics, including the patch diameter (D), equivalent length proposed by Mazda (L_E), and an effective diameter D_{eff}. A universal empirical curve describing the drag coefficient based on (L_E) and D_{eff} is also presented. It was found that the effective diameter was able to capture competing parameters including patch diameter, porosity, and cylinder diameters into a single parameter to obtain the drag coefficient of the physical models. The results revealed that the time-average drag coefficient decreased with an increased Reynolds number and porosity. It was found that the ratio of $\frac{C_D}{\mathrm{St}}$ to the blockage parameter ($C_D a D$) exhibits a linear relationship, indicating that the parameter $\mathrm{St} a D$ is constant for all patches considered. This finding was also valid using equivalent length and effective diameter as the characteristic lengths. In addition, based on time-resolved PIV results downstream of the physical model, we found that the vorticity magnitude decays and the vortex structure is more streamlined with an increase in porosity. This analysis of the hydrodynamics of mangrove rootlike models can also be extended to predict values of drag coefficient in other canopy flows, including submerged arrays, flexible elements, and bio-inspired coastal infrastructures.

DOI: 10.1103/PhysRevFluids.3.073801

I. INTRODUCTION

Mangroves provide many natural benefits, including shoreline protection, coastal ecosystem habitat, shoreline protection, and water filtration [1–5]. Mangrove roots exhibit complicated hydrodynamics, with some areas of mangrove growth benefiting from vegetated shorelines, while

*ocuret@fau.edu

FIG. 1. Prop roots of red mangroves (*Rhizophora mangle*). Mangrove roots involve a complex system, comprising intricate, long tidal creeks, and surrounding mangrove swamps which form heavily vegetated floodplains. The roots buffer against damage to coastal communities and provide services such as nursery areas for fish production, biodiversity, and carbon sequestration. Scales in the figures are approximate values.

other areas are exposed to scouring and sediment erosion [6]. In many cases, the roots trap sediments flowing down rivers and off the land, which helps to stabilize the coastline and prevent scouring and erosion from waves and storms [3,7]. In particular, the morphological characteristics of red mangroves (*Rhizophora mangle)* may be strongly linked to their survival under environmental conditions (Fig. 1) [8,9]. Red mangroves' robust network of roots withstands extreme environmental conditions and can provide an effective model for bio-inspired applications in shorelines [8,10–13]. An improved understanding of the hydrodynamics of mangrove roots will facilitate the incorporation of bio-inspired mangrove-like structures for erosion control, coastal protection, and habitat reconstruction. As such, it is vital to characterize the fluid dynamics of the mangrove roots under different flow conditions to quantify how the flow structure would interact with mangrove-like models. In particular, the motivation of this work is to understand the hydrodynamics of mangrove roots in unidirectional flow using a patch of rigid circular cylinders as a simplified model. Our main research questions are:

(1) How does porosity affect the mean values of the total streamwise drag force acting on the porous cylinder based on different length scales?

(2) How does porosity influence the wake structure of a porous patch of cylinders in the mean and instantaneous flow field?

The flow in a mangrove creek is heavily dependent on the creek depth and the mangrove site location. Horstman *et al.* [14] performed field measurements at the north section of Mae Nam Trang Creek in the Kantang estuary in Trang province in Thailand and found that inside the mangrove swamps water flowed nearly parallel to the corresponding mangrove swamp for shallow water depths ranging from 7 to 150 cm [14]. Similarly, Wolanski [15] conducted field observations of water current within heavily vegetated swamps and reported that peak tidal velocities at 50 m away from Coral Creek in Australia were less than 7 cm/s in water shallower than 1 m depth. Katherisan [16] observed water flow in the Vellar Estuary on the southeastern coast of India and found that tidal velocities within the mangrove swamps were roughly 9 cm/s compared to nonmangrove bank areas where the velocities were between 18 and 20 cm/s in 1.5 m water depth. In Everglades National Park, Florida, velocities of less than 20 cm/s were found in the red mangrove areas at about 1 m water height above the bed [17–19].

In terms of root morphology, the prop roots found in the species of *Rhizophora* highlight the most recognizable feature of mangroves and can be characterized by their geometrical properties (Fig. 1). The established mangrove roots consist of rigid roots attached to the trunk and fixed to

the soil, whereas newer and more flexible stems or roots hang from the upper branches and move back and forth with tidal currents [8,11,20–22]. Mazda *et al.* [23] obtained measurements of trunks, prop roots, and their geometrical characteristics, such as root heights and root system widths of red mangroves (*Rhizophora*) in the field. Values of porosity were reported as low as 55% in mangroves with mean trunk diameter in the range of 4–9 cm [7].

The flow structure in mangrove forests has implications for the transport and distribution of sediments and nutrients. Tinoco and Coco [24] investigated the onset of sediment resuspension under currents and wave conditions with submerged arrays of sparse and dense rigid cylinders. Bouma *et al.* [6] performed field study and laboratory analysis of currents through fully submerged patches of bamboo sticks to examine sediment transport and erosion on tidal marshes and reported maximum sediment accumulations within the patches. Norris *et al.* [25] derived turbulence patterns due to the presence of vegetation and studied the effect of sediment properties on regional morphodynamics. The distribution of water velocity and turbulence intensity in the wake of a porous obstruction can impact sediment deposition.

To date, a few studies have been conducted on flow structure and drag force on mangrove prop roots. These studies have identified a range of mangrove root hydrodynamic properties [10,26–28]. Struve *et al.* [29] investigated the influence of mangroves on flow hydrodynamics in a flume using dowel rods which were fitted with curved extensions to simulate the roots of the *Rhizophora* species. They found that the most important factors influencing flow velocity are tree diameter and density. Previous studies on mangrove hydrodynamics indicate that the complex circulation generated in water through mangrove roots dominates the flow friction. Furukawa *et al.* [7] found that mangrove roots generate complex two-dimensional current fields and regions with jets, eddies, root-scale turbulence, and stagnation. Additionally, Mazda *et al.* [23] applied the momentum equation to obtain a balance between the water surface slopes and drag force in pristine mangrove swamps. They found that the drag coefficient of prop roots decreases with increasing values of Reynolds number from $C_D = 5$ for $\mathrm{Re} < 1 \times 10^4$ to $C_D = 0.4$ for $\mathrm{Re} > 5 \times 10^4$. Mazda *et al.* [23] and Furukawa *et al.* [7] conducted field measurements and characterized the flow through mangrove roots in tidal currents. They reported that mangrove roots are very similar to circular cylinders of uniform diameter d. To further understand the fluid dynamics around mangrove roots, we performed a series of experiments varying key parameters of mangrove roots including length scale and porosity.

In a circular patch formed by the arrangement of multiple cylinders, the drag coefficient depends on various factors including geometrical configuration and spacing between cylinders, as well as flow speed and fluid properties. Although the drag coefficient of a canonical cylinder is well documented in the literature, it is not well understood for a circular patch. Petryk [30] showed that when cylinders are densely packed, the mean drag on the entire patch of cylinders could be either smaller or greater than that for a single cylinder depending on the orientation of the cylinders. Most researchers have measured surface slope to estimate the drag force indirectly [31–34]. They estimated drag force using a simplified momentum equation and surface water slope measurement. However, this approach neglects flow unsteadiness produced by complex cylinder wake interactions that occur when multiple cylinders are placed in close proximity, generating strong local velocity and pressure gradients between the cylinders. Thus, indirect force estimation could be prone to a high level of uncertainty due to the strong local gradient of velocity, in both pressure and viscous drag, and the overall unsteady nature of the problem. Therefore, direct force measurements are more precise to measure and analyze the drag force.

The flow structure in the wake of a patch of cylinders is not only a function of porosity, but also other flow and geometrical parameters, including Reynolds number, the patch and root diameter, and the arrangement of the cylinders in the patch and drag coefficient. Since the network of roots is a combination of individual roots with different diameters (porosities) and spacing between them, the flow structure is impacted by the porosity and spacing ratio. Spacing ratio (L/d) is the ratio of the distance between the center of two adjacent cylinders to the cylinder's diameter [Fig. 2(c)].

While previous studies have examined the wake region behind a porous patch [31,33–35], here we focus on the relationship between force, flow field, and analysis of appropriate length scale to

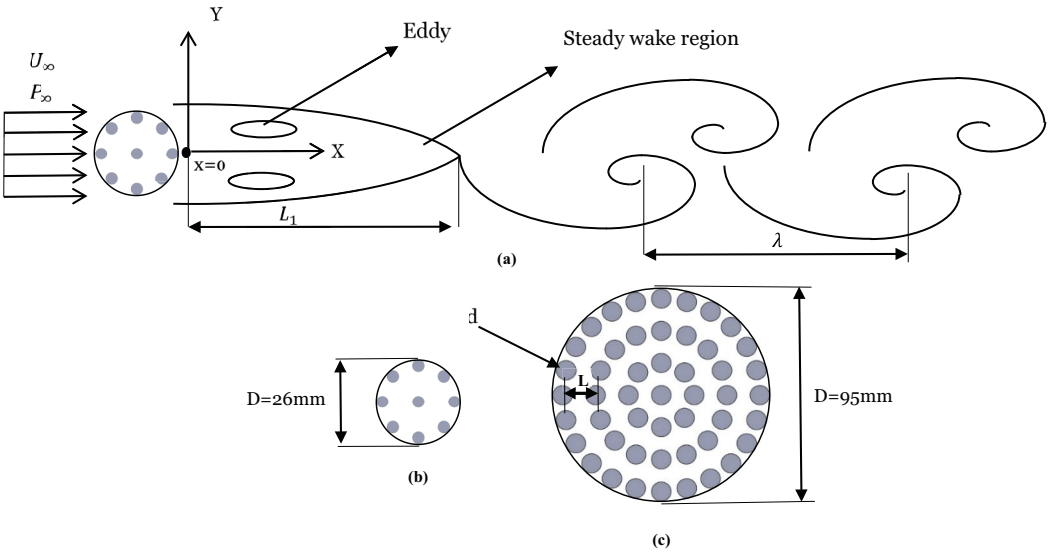

FIG. 2. Schematic of the flow field (a) and physical models (b), (c). (a) Sketch of the mean flow structure around a circular patch of the cylinders. The flow patterns are characterized by the formation of the symmetrical steady wake region in the near wake. The length of the steady wake, $\boldsymbol{L}_1$, is measured from the back of the cylinder in the streamwise direction. Wavelength of the vortex shedding (λ), defined as the distance between two sequences of vortex shedding (b) Patch configuration for cases 1–3. (c) Patch configuration for cases 4–7.

describe the problem. Prior work by Zong and Nepf [34] has studied the flow structure behind finite circular patches and described the wake behind a circular staggered patch by dye visualization. Using a patch of multiple cylinders, they measured drag indirectly by calculation of momentum balance in the centerline. Zong and Nepf measured the wake flow in a longitudinal direction with acoustic Doppler velocimetry. This technique is limited to a point measurement of the flow field so that the measurements of velocity distributions in the wake are considered in several locations.

The problem of flow through mangrove roots or a patch of cylinders has been characterized by using different length scales, including the root diameter and patch diameter [Figs. 2(b)–2(c)]. Different authors mention various length scales to report drag coefficients for fluid dynamics around vegetation. Prior research has mostly used the individual root diameter *(d)* as the length scale [31,34–36]. However, in a porous cylindrical patch composed of smaller roots, the patch diameter and spacing between stems is also commonly used as a characteristic length scale for the drag coefficient and the vortex shedding frequency. Therefore, drag coefficient for a patch of cylinders with a constant patch diameter changes with porosity. Mazda *et al.* [23] proposed a vegetation length scale, L_E, that is based on the projected area and volume of mangrove vegetation to define the drag coefficient based on that length scale.

Each of the previously mentioned length scales has some limitations. For example, the length scale of a circular patch of cylinders based on the outer diameter, D, does not incorporate porosity and its effect on the drag coefficient and the wake structure. Mazda's length scale, L_E, is based on the solidity of a control volume surrounded by the mangrove and does not take into account root configurations, cylinder shape, or arrangement. The length scale of the root diameter, d, does not reflect the spacing or configuration of the multiple roots or cylinders.

In this work, we consider and investigate the effect of porosity on the flow downstream of the patches of the rootlike cylinders in the middepth of a water tunnel. A new length scale, the effective diameter, is proposed that represents the diameter or length scale obstruction "seen" (or experienced) by the flow. An empirical universal drag coefficient is presented based on a new length scale, the effective diameter. We also compare drag measurements based on patch length scales (D), Mazda

length scale (L_E), and effective diameter (D_{eff}). We provide a more detailed description of the unsteady wake structure using particle image velocimetry (PIV) measurements with high spatial resolution. Our objective is to focus on the flow behind the mangrove roots in the horizontal wake plane through PIV, which allows for nonintrusive multipoint measurements of the flow field and an examination of the relationships between direct force measurement and flow structure. Although our analysis is based on mangrove models, it can also be applied to other underwater vegetation or flow through porous-bluff objects.

II. METHODS

By assuming a two-dimensional x-z flow, where x, y, and z are orthogonal coordinates, x is positive in the direction of the mean flow, y is the horizontal, spanwise direction, and z is vertical upwards [Fig. 2(a)], with their respective velocities u, v, and w, the temporally and horizontally averaged streamwise momentum equation is written as

$$\frac{\partial\langle\bar{u}\rangle}{\partial t}+\langle\bar{u}\rangle\frac{\partial\langle\bar{u}\rangle}{\partial x}+\langle\bar{w}\rangle\frac{\partial\langle\bar{u}\rangle}{\partial z}$$
$$=-\frac{1}{\rho}\frac{\partial\langle\bar{p}\rangle}{\partial x}-\overbrace{\left(\frac{\partial\langle\overline{u'u'}\rangle}{\partial x}+\frac{\partial\langle\overline{u'w'}\rangle}{\partial z}\right)}^{\text{Reynolds stress}}+\upsilon\frac{\partial^2\langle\bar{u}\rangle}{\partial z^2}-\underbrace{\left(\frac{\partial\langle\overline{u''u''}\rangle}{\partial x}+\frac{\partial\langle\overline{u''w''}\rangle}{\partial z}\right)}_{\text{Dispersive stress}}-f, \tag{1}$$

where spatial average terms are defined with a bracket, and time-averaged terms are shown with bar. Reynolds stress terms, as well as velocity field, are discussed for the mangrove-like models presented. In the simplest case, with rigid cylinders and a constant drag coefficient over the full water depth, the flow can be considered two-dimensional. In addition, some other works [32,34,36] simplified Eq. (1) to obtain the force measured through water slope method. However, this method neglects Reynolds stress and dispersive terms, resulting in potential inaccuracies in the calculated drag force.

In this work, we measured the drag force experienced by the entire patch and then calculated the drag coefficient based on the three length scales: patch diameter D, Mazda length scale L_E, and the effective diameter D_{eff}. Drag coefficient is defined as

$$C_D=\frac{F}{0.5\rho U^2 h L_c}, \tag{2}$$

where F is an average drag in the direction of the mean flow, ρ is the fluid density, L_c is the characteristic length, U is the free-stream velocity, and h is the water depth.

Figure 2(a) shows the schematic of the flow structure behind a circular patch of cylinders and the parameters used in this work. Flow passes through the patch and a region of steady wake forms immediately in the downstream. There are small-scale eddies formed in this region, and the streamwise velocity decreases to its minimum value [37]. The steady wake length L_1, is defined as the streamwise distance from the back of patch to minimum velocity point. Downstream of this point, a large-scale von Kármán vortex shedding initiates. The wavelength of the vortex shedding, λ, is defined as the distance between two sequences of vortex shedding.

III. PHYSICAL MODELS

We considered three patches of cylinders with the same outer diameter (D) of 2.54 cm and with different individual cylinder diameters. There were nine cylinders for cases 1 to 3 and 49 cylinders for cases 4 to 7. The arrangement and the properties of each case are depicted in Figs. 2(b) and 2(c) and Table I, respectively. We considered a range of spacing ratios from 1.5 to 4.8 (Table I). For a

TABLE I. Main geometrical and flow variables of experiment cases. For each case, experiments were run for five different upstream velocities from 2.3 to 11.9 cm/s corresponding to Reynolds number, based on the patch diameter, ranging from 600 to 12 000. a is frontal area per unit volume and is defined as $a = \frac{1}{V}\sum_{i=1}^{N} A_i$ where A_i is a frontal area of indivdual clinders and N is the number of cylinders. L_E is characteristic length scale calculated based on the ratio of solid to the frontal area, and porosity is calculated by $\varphi = 1 - N(\frac{d}{D})^2$. There were nine cylinders for cases 1 to 3 and 49 cylinders for cases 4 to 7.

Case	Frontal area (a) (mm^{-1})	Patch diameter (D) mm	aD	Root diameter (d) mm	Porosity % (φ)	Solidity % (β)	Spacing ratio ($\frac{L}{d}$)
1	107.6	26	2.86	6.35	47.1	52.9	2
2	80.7	26	2.14	4.76	70.4	29.6	2.67
3	53.82	26	1.43	3.17	86.5	23.5	4
4	65.8	95	6.25	9.52	50.7	49.3	1.5
5	43.89	95	4.17	6.35	78.1	21.9	2.3
6	32.9	95	3.12	4.76	87.6	12.4	3.1
7	21.2	95	2.08	3.17	94.5	5.5	4.8
8 (Chen *et al.* [32])	7.9	120	0.9	6.4	96	4	–
9 (Tinoco and Cowen [39])	4	106	4.24	3.1	99	1	4.83

given water depth, the porosity of the mangrove root system was computed based on the ratio of the submerged root volume to the total defined volume to calculate the drag force induced by the presence of mangrove roots.

Below, we define Reynolds number, Re, Strouhal number, St, and drag coefficient, C_D, based on three different length scales: patch diameter, D, equivalent length, L_E, and effective diameter, D_{eff}. For the patch diameter, the nondimensional numbers were defined as

$$\text{Re}_D = \frac{\rho U D}{\mu}, \tag{4}$$

$$St_D = \frac{f D}{U}, \tag{5}$$

$$C_D = \frac{F}{0.5\rho D h U^2}, \tag{6}$$

where the subscript D specifies the length scale, ρ is the fluid density, U is the freestream velocity, μ is the fluid viscosity, f is the frequency of the vortex shedding, F is the drag force, and h is the height of the submerged portion of the patch.

Mazda *et al.* [23] proposed a mangrove characteristic length L_E as a function of the projected area of mangrove vegetation in a squared volume of the vegetation and defined the characteristic length scale as

$$L_E = \frac{V_{\text{total}} - V_{\text{fluid}}}{A} = \frac{V_{\text{solid}}}{A}, \tag{7}$$

where, V_{total}, V_{fluid}, and A are the squared control volume enclosing the patch, the fluid volume in the patch, and the frontal area, respectively. By applying the above equations for a circular patch composed of multiple cylinders and using the solidity [volume occupied by cylinders over the total

patch volume of a squared control volume ($\beta = N\frac{\pi}{4}(\frac{d}{D})^2$], the following terms can be defined:

$$L_E = \frac{N\frac{\pi d^2}{4}h}{Dh} = N\frac{\pi d^2}{4D}, \tag{8}$$

$$\frac{L_E}{D} = N\frac{\pi}{4}\left(\frac{d}{D}\right)^2 = \beta = 1 - \varphi, \tag{9}$$

where β is the solidity of the patch (or the volume occupied by the cylinders), φ is the porosity (volume not occupied by the cylinders), and N is the number of cylinders. Therefore, the characteristic length can be rewritten as

$$L_E = D\beta = D(1 - \varphi). \tag{10}$$

The Reynolds number and Strouhal number based on the L_E characteristic are defined as

$$\mathrm{Re}_{L_E} = \frac{\rho U L_E}{\mu} = \frac{\rho U D}{\mu}(1 - \varphi), \tag{11}$$

$$C_{D\,L_E} = \frac{F}{0.5\rho L_E h U^2}. \tag{12}$$

The effective diameter length scale was defined based on the wake signature instead of a physical length scale. The frequency of the vortex shedding generated by the patch was compared against an equivalent solid cylinder that produces the same wake signature. In other words, the Strouhal number of the patch was matched with an equivalent Strouhal number of a solid cylinder. By this comparison, a "solid" effective diameter was determined for the patch. This effective diameter can be described as the obstruction experienced by the fluid flow. Thus, the "effective diameter" is the diameter of an individual solid cylinder that gives the same frequency of vortex shedding as generated by the patch. We define the effective diameter by

$$D_{\mathit{eff}} = \frac{\mathrm{St}_{\mathit{eff}} U}{f}, \tag{13}$$

where $\mathrm{St}_{\mathit{eff}}$, is the Strouhal number of a solid cylinder, which approximately equals 0.2:

$$\mathrm{Re}_{\mathit{eff}} = \frac{\rho U D_{\mathit{eff}}}{\mu}, \tag{14}$$

$$C_{D_{\mathit{eff}}} = \frac{F}{0.5\rho D_{\mathit{eff}} h U^2}, \tag{15}$$

where the subscript *eff* indicates effective diameter.

IV. EXPERIMENTAL SETUP AND INSTRUMENTATION

We carried out a series of experiments in a closed-loop water flume with a length, width, and depth of 2, 0.25, and 0.25 m, respectively. A schematic of the experimental setup is shown in Fig. 3. The physical models were vertically mounted on an air-bearing system. The air-bearing system was used to support the physical models while minimizing friction forces to conduct precise force measurements. The distance from the water channel inlet to the models was 70 cm. A 9-N load cell (Futek LSB200) was attached to the mount of the physical model to measure the drag force of the entire model. The depth of the submerged portion of the cylinders was 22 cm. The cylinders were assembled with a tight fit through the end plates and with negligible clearances to prevent any deflections at either end [Fig. 3(b)]. For drag measurement of the endplate, it was attached to the load cell through a short rigid extension with negligible drag force. The endplate drag force was

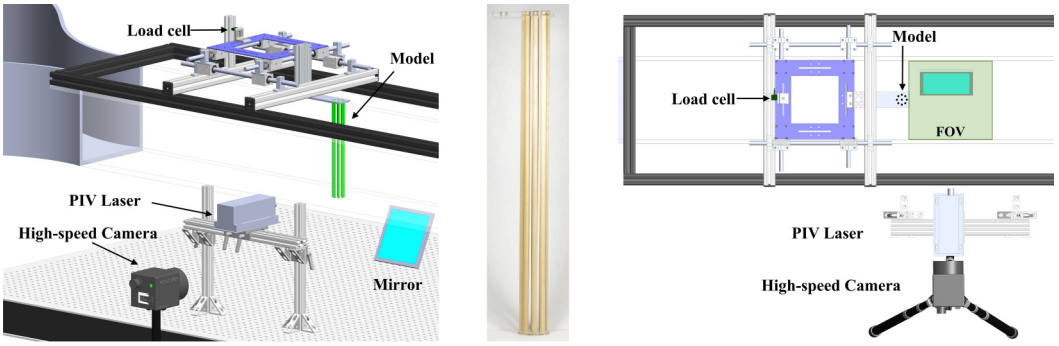

FIG. 3. Schematic of experimental setup and field of view (FOV) located in the middepth. Isometric view of the experimental setup (a) picture of one physical model (b) top view of the experimental loadcell (c). The closed-loop water tunnel cross section is 25 cm × 25 cm with the blockage ratio of 10%. The setup includes a recirculating flume, an air-bearing system to mount the models, a load cell, a high-speed camera, and a laser to perform PIV measurements. A 45° mirror was used to have a bottom-up view of the flow field. The velocities in the streamwise and spanwise directions are denoted by u and v, respectively.

measured after a quasisteady state was achieved ($T = 0$) and the endplate drag force was subtracted from the total drag on the entire patch. The distance between cylinder bottoms and the flume bed was less than 1 mm to minimize the three-dimensional flow effects. The blockage ratio in the test section, defined as the patch diameter divided by channel width, was around 10%. The upstream flow velocity was adjusted from 2.3 to 11.9 cm/s corresponding to Reynolds number of 600 to 3000 based on patch diameter, respectively.

The velocity flow field was measured using PIV. To conduct the PIV measurements, the water was seeded with hollowed-glass spherical particles with a diameter of 10 μm. The particles were illuminated with a continuous 5-W laser (continuous wattage lasers PIV01251) with a 532 nm wavelength. The motion of the particles was recorded using a high-speed camera (Photron Fastcam Mini UX50) with a resolution of 1280 × 1024 pixels at 125 frames per second and shutter speed of $\frac{1}{1250}$ sec. The acquired PIV data were processed using TSI Insight 4G software. The images were preprocessed with a Gaussian filter and subtracted from the background. A Nyquist grid and fast Fourier transform correlator was used for the PIV analysis. In addition, the postprocessing includes local validation (median test method) and vector conditioning with neighborhood size 3 × 3 pixels.

The velocity vector field was computed from particle displacement with a fixed elapsed time for two sequential images. The measured flow velocity without models indicated that the turbulence intensity of the free stream was less than 0.5%. The turbulence statistics of the flow were estimated from the PIV flow measurement. The Strouhal number was computed based on the peak value of the signal in the frequency domain from the PIV measurements. Three minutes were required to reach a quasisteady state and initiate periodic vortex shedding. The initial time, $T = 0$, was defined after quasisteady state was achieved ($T = 0$).

V. RESULTS

A. Force results

Figure 4(a) shows the mean drag force as a function of free-stream velocity. The results follow closely the expected quadratic power law of drag with respect to the upstream velocity. The dominant nondimensional wake shedding frequency is described by Strouhal number, $\mathrm{St} = \frac{fD}{U}$. Figure 4(b) shows that Strouhal number increases with porosity and only has a minimal variation with Reynolds numbers. This result shows the strong dependency of the vortex shedding frequency on the patch

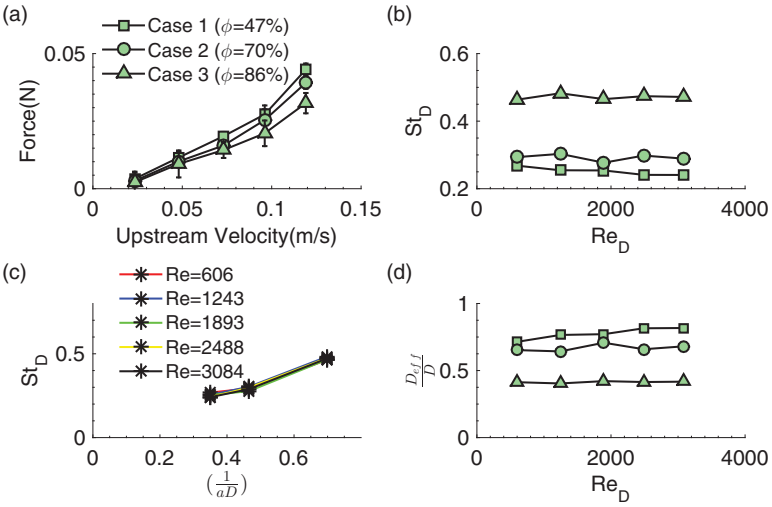

FIG. 4. (a) Drag force measured on the entire patch with respect to the upstream velocity. (b) Variation of Strouhal number, based on patch diameter versus Reynolds number. Strouhal number increases by porosity growth. (c) Strouhal number increases with $\frac{1}{aD}$ for different Reynolds numbers. (d) Effective diameter normalized by patch diameter as a function of Reynolds number.

porosity. For a porosity of 86% (case 3), the Strouhal number is approximately 0.45. This Strouhal number value is more than twice that of a solid single cylinder.

Figure 4(c) shows that Strouhal number increases with the inverse of aD for all Reynolds numbers, thus indicating a dependency of Strouhal number with the patch frontal area. Figure 4(d) displays the effective diameter normalized by the patch diameter, $\frac{D_{\text{eff}}}{D}$, as a function of Reynolds number based on the patch diameter. As the porosity increases (less solidity) the normalized effective diameter also decreases.

B. PIV results

In this section, time-averaged flow pattern for the streamwise velocity, vorticity, Reynolds shear stress, and total mean turbulence intensity associated with the dynamics of the vortex structure for three different porosities (cases 1–3) are presented. In addition, the time evolution of flow patterns is described and compared to different time instants. Even though the flow measurements were conducted at five Reynolds numbers (Re = 600, 1250, 1900, 2500, and 3000), only the results at $\text{Re}_D = 3000$ are presented since the flow characteristics and main flow features were similar for all cases.

Figures 5(a)–5(c) present the streamwise velocity downstream of the patches with $\varphi = 47\%$, 70%, and 86%, respectively. For the three cases, a steady wake region is formed toward the end of the patch. As the porosity increases, the velocity deficit behind the model decreases. However, the steady wake length increases with porosity (this result is more evident from Fig. 7).

The vorticity contours of the porous patches are shown in Figs. 5(d), 5(e), and 5(f). The vorticity pattern for case 1 (the least porous patch) shows that two negative and positive areas emerge in the near wake and extend around two diameters length downstream of the patch. These areas evolve in the near wake and produce swirling flow. In contrast, at larger porosities, the vortices interact over a long distance and the region of intense vorticity wake expands. The result shows that not only did the vortex structure shift, but the intensity of vorticity was weakened from 13.56 to 3.52 1/s with increasing the porosity.

Reynolds shear stress term, $(-u'v')$ where u' and v' are the fluctuating streamwise and transverse velocity components respectively, is a parameter that implies unsteady drag force acting on the

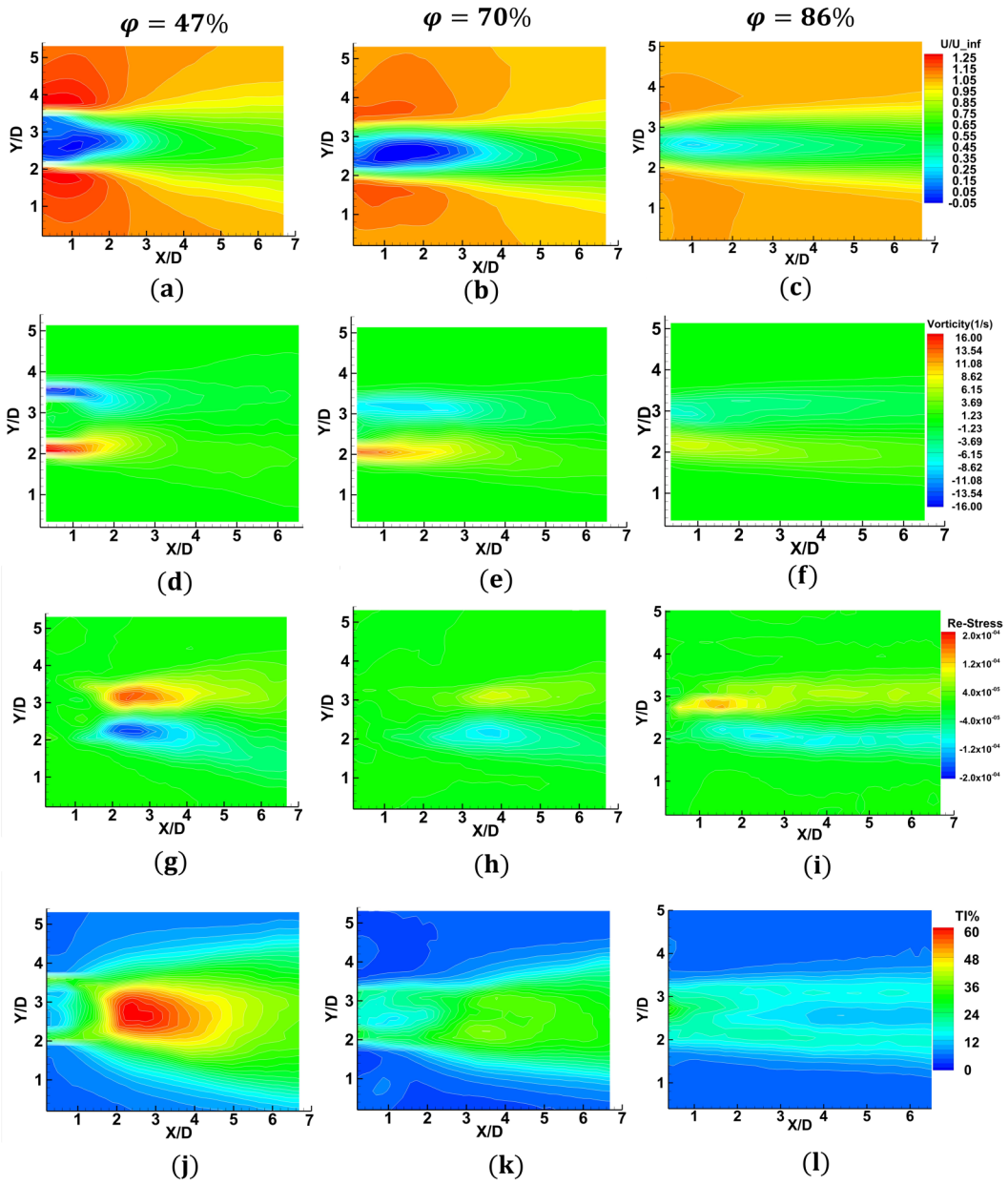

FIG. 5. Time-average flow fields for different porosities. Left column: case 1, $\varphi_1 = 47\%$; middle column: case 2, $\varphi_2 = 70\%$ and right column: case 3, $\varphi_3 = 86\%$. (a)–(c) Streamwise velocity; (d)–(f) contour of vorticity; (g)–(i) contour of Reynolds stress; (j)–(l) contour of turbulence intensity (TI). All results are at Re = 3000 with time step $\Delta t = 0.008$ s and $T = 0.568$ s.

entire patches. The patterns of time-averaged Reynolds shear stress are presented in the third row of Fig. 5. The wake expansion can also be explained by examining the Reynolds stress contours $(-u'v')$ [Figs. 5(g)–5(i)]. The red and blue regions correspond to negative and positive Reynolds stress, respectively. There is a noticeable weakening of the Reynolds stress intensity (80%) as a result of increased porosity (39%), leading to approximately (30%) drag coefficient reduction on the entire

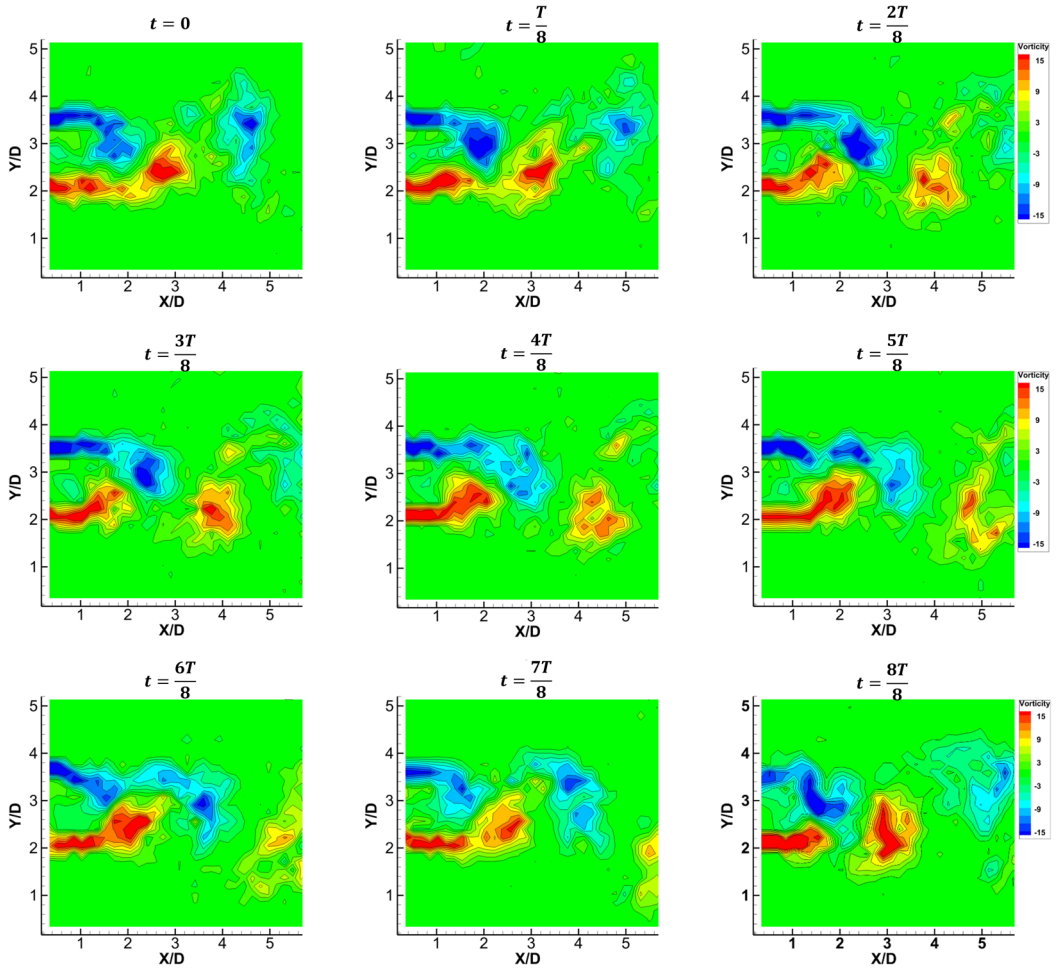

FIG. 6. The instantaneous z-vorticity field for Re = 3000 and $\varphi = 47\%$ at different time instants. $T = 0.568$ s is the time of one vortex shedding period. The features of time-resolved vorticity field indicate that the von Kármán vortex street behind the porous patch has a shorter period time compared to a canonical cylinder ($T = 1.2$ s).

patch. The peak values of Reynolds stress are seen to shift downstream, and their magnitudes are considerably diminished for larger porosities.

Another important physical parameter is the mean turbulence intensity evaluated from the fluctuating component of velocities in the streamwise direction. The mean turbulence intensity is defined by $\frac{U_{\text{rms}}}{\bar{U}}$ where $\bar{U}$ is the time-averaged (mean) velocity and U_{rms} is the root mean square of streamwise velocity fluctuations ($U_{\text{rms}} = \sqrt{\overline{u'(t)^2}}$). The time-averaged total mean turbulence intensity is presented in Figs. 5(j)–5(l). The turbulence intensity is greater in the near wake of the dense patch. However, there is an evident decay in the turbulence intensity as the porosity increases, in addition to a decrease in the velocity gradients.

The vorticity field at various time instants is displayed in Fig. 6 to depict the unsteady behavior of the wake flow behind the physical model (case 1). From Fig. 6, we recognized that positive and negative vortex structures both exist in the interference flow zone at various time steps. We observed the generation of a small-scale turbulent wake region directly behind the porous patches. In this

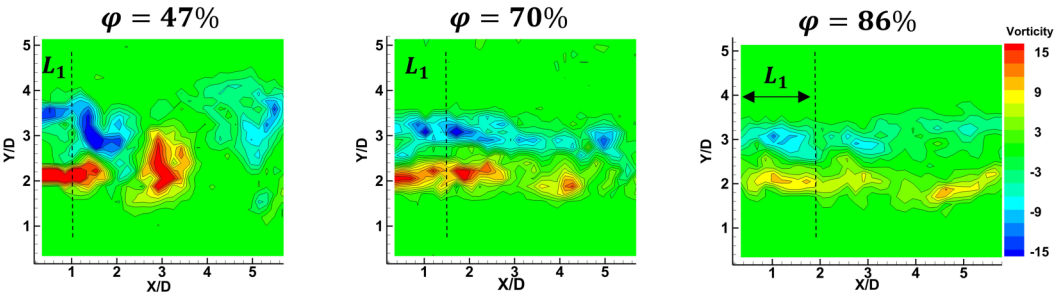

FIG. 7. The effect of porosity of patch on the time-resolved vorticity field. The panels compare the vertical vorticity magnitude behind the patch for $\varphi = 47\%$, $\varphi = 70\%$, and $\varphi = 86\%$ at the vortex shedding period ($T = 0.568$ s) for Re $= 3000$. The vortices in the separated shear layers at $\varphi = 47\%$ create coherent vortex structure. The steady wake length L_1, is defined as the streamwise distance from the back of patch to minimum velocity point. Greater porosity increases L_1 and λ (detached vortex wavelength).

region, the vortices are turbulent [based on Figs. 5(j)–5(l)], and eddies begin to interact directly after passing the patch downstream of the roots. The small turbulent vortices recombine into larger vortex structures forming the von Kármán vortex street.

At $t = \frac{T}{8}$, due to the influence of cylinders in the patch, a negative vortex structure with high intensity (around -15 1/s) appeared behind the patch ($x = 0$). Owing to the vigorous shear layer interactions, small vortices were generated in the wake downstream until around $\frac{X}{D} = 2$, where they recombine together. At $t = \frac{3T}{8}$, the vortex detached from the steady wake surface, and the negative vortex appeared near $\frac{Y}{D} = 3$ with high intensity. There was a positive vortex structure near the lower surface of the patch with a slightly reduced intensity. When the patch was at time instant $t = \frac{T}{8}$, $\frac{4T}{8}$, and $\frac{8T}{8}$, the intensity of both positive and negative vortices was significantly augmented (around 50%) compared to their previous time instants. When vortices evolved to $t = \frac{8T}{8}$, the position of positive vortex structure in the flow field was similar to that in $t = \frac{T}{8}$, but the intensity was slightly increased. The features of the above discussed time evolution show that the von Kármán vortex street forms after $\frac{X}{D} = 2$ from the patch, and the period of vortex shedding ($T = 0.568$ s) is about half of the canonical cylinder period time ($T = 1.2$ s) with the same diameter.

Figure 7 compares the vorticity field at the same time interval ($T = 0.568$ s) for different porosities. It showed that for the least porosity, the greatest value of the vorticity occurred toward the end of the steady wake region, where interaction between the separated shear layers of the porous cylinder resulted in the formation of vortices. The vorticity magnitude behind the patch decayed with an increase in porosity and vortex structure is more streamlined in the downstream wake. This could be because as the porosity increases, the separated shear layers get longer, and the strength of the exit flow at the back of the patch increases sufficiently so that the lateral movement of the end of one shear layer toward the other layer is impeded. Therefore, the vortices rotate in opposing direction and suppress the formation of vortex street in the steady wake region. After L_1, large-scale eddies form through merging of neighboring eddies and contain vorticity of the same sign with greater magnitude than in upstream vortices. After they merge, the small energetic votices billow in the downstream wake which causes to increase L_1 with porosity.

VI. DISCUSSION

A drag coefficient is used to describe the resistance of the fluid to flow through the mangrove rootlike models. Figures 8(a)–8(c) show the drag coefficient based on the patch diameter, Mazda length scale (L_E), and effective diameter (D_{eff}). For the patch diameter length scale shown in Fig. 8(a), we can observe a similar trend for all cases: that the drag coefficient decreases with Reynolds number and tends to reach a constant value for high Re. This trend can also be observed in the drag coefficient

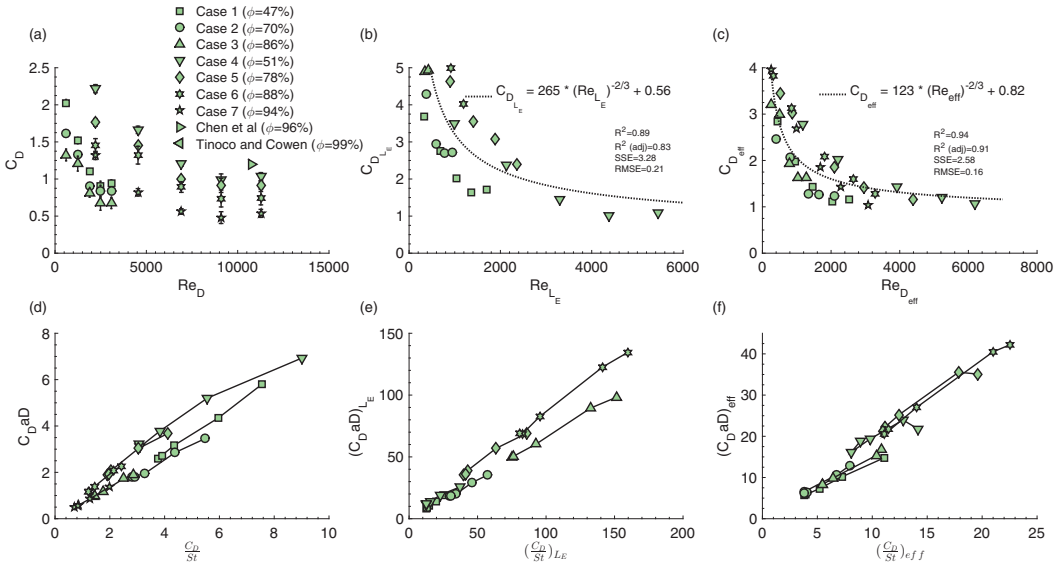

FIG. 8. Total drag coefficient as a function of Reynolds number based on patch diameter (a), equivalent length L_E (b), and effective diameter (c). Vertical bars show the 95% confidence interval. (d), (e), (f): Blockage ratio ($C_D aD$) vs energy released per vortex shedding based on patch diameter (d), equivalent length (e), and effective diameter (f).

of a solid cylinder. This trend is similar to the drag coefficient of a solid cylinder. However, there is an evident spreading of the data at a given Re for different porosities.

The results show that as porosity increases the drag coefficient decreases. This decrease in drag is most likely due to the adverse pressure gradient for the low porosities that acts on the porous patch, which makes the total drag coefficient become nearly equal to that of a solid cylinder of diameter D, with an additional drag acting on the interior cylinders due to the bleeding flow advected through the patch. Therefore, C_D is a function of both Reynolds number and porosity.

Below is the drag coefficient of a canonical cylinder described by the empirical expression [38]

$$C_D = 1 + 10\mathrm{Re}^{-2/3}, \quad 1 < \mathrm{Re} < 10^5. \tag{16}$$

In particular, C_D decreases with increasing Reynolds number up to $\mathrm{Re} = 1000$. In moderate Re number range (10^3 to 10^5) the drag remains relatively constant until it decreases when the boundary layer becomes turbulent (3×10^5), and it starts to increase slowly with Re. In contrast, for a patch of circular cylinders, drag coefficient reduces constantly until $\mathrm{Re} \approx 10^4$ and stays almost unchanged after $\mathrm{Re} > 10^4$.

The drag coefficient based on the effective length introduced by Mazda *et al.* [23] is shown in Fig. 8(b). The trend is similar to the drag coefficient based on patch diameter as it decreases with Reynolds number and seems to reach a constant value for a high Reynolds number. Even with an appreciable difference in the drag coefficient for a given Re number, a common trend can be observed. The dotted line in Fig. 8(b) is given by the following curve fit:

$$C_{DL_E} = 0.56 + 265\mathrm{Re}_{L_E}{}^{-2/3}, \quad 83 < \mathrm{Re}_{L_E} < 5800. \tag{17}$$

Figure 8(c) shows the drag coefficient based on the effective diameter as a function of $\mathrm{Re}_{D_{\mathrm{eff}}}$. Similar to the drag coefficient based on previous length scales, $C_{D_{\mathrm{eff}}}$ decreases with Reynolds number until it seems to approach a constant value. However, compared to the previous two length scales, the data suggest that using effective diameter as the length scale helps to collapse the drag coefficient values to a uniform curve.

The drag coefficient based on the D_{eff} approaches one after $1500 \leqslant \text{Re}_{\text{eff}} \leqslant 6400$ [Fig. 8(c)], consistent with the C_D of a single cylinder at an intermediate Reynolds number. This finding indicates that the effective diameter is able to capture competing parameters—patch diameter, porosity, and cylinder diameters—into a single parameter to obtain the drag coefficient of the physical model.

The universal curve fit based on effective diameter length scale is given by

$$C_{D\text{eff}} = 0.82 + 123\text{Re}_{\text{eff}}{}^{-2/3}, \quad 443 < \text{Re}_{\text{eff}} < 6400. \tag{18}$$

As a guideline, one can calculate effective patch diameter by measuring the streamwise velocity and vortex shedding frequency at twice the diameter downstream of the patch, where the von Kármán vortex street initiates. Then the effective Reynolds number can be obtained [Eq. (14)] to predict the effective drag coefficient of the patch from the universal curve fit [Eq. (18)].

The total drag coefficient is the sum of viscous and pressure drag advected by the turbulent wake downstream of the patch. Reynolds number based on Mazda length scale (Re_{L_E}) ranges from 83 to 5800, and viscous drag dominates the flow due to the strong gradient of local velocity. Therefore, the total drag coefficient is much greater based on Mazda's length scale [Fig. 8(b)] compared to the effective diameter length scale, in which the Reynolds number changes from 443 to 6400, and viscous drag has a relatively minor contribution.

By assuming the universal curve fit is valid for greater Reynolds values ($10^4 < \text{Re}_{L_E} < 10^5$), the curve has a horizontal asymptote at $C_D \cong 0.56$. The drag coefficient obtained by the curve fit [Eq. (17)] falls around 6% difference from the field work by Mazda *et al.* [23] where they found $C_D \cong 0.6$ for $\text{Re} = 5 \times 10^4$. The curve fit is in good agreement with the calculated data ($R^2 = 0.89 \pm 0.05$). The Mazda length scale is based on the ratio of solid to total volume and can approach zero. However, the effective diameter, which is based on the flow characteristics, has a limit of 0.82.

The drag reduces significantly as the porosity increases in part because the shear layer interaction weakens [Figs. 5(a)–5(c)]. Increasing the porosity also decreases the vorticity gradient [Figs. 5(d)–5(f)], with a decrease in momentum flux (associated with Reynolds stress [Figs. 5(g)–5(i)] and consequent drag forces.

Tinoco and Cowen [39] and Chen *et al.* [32] estimated the drag force from Tanino and Nepf [7] based on solidity and the Reynolds number (based on stem diameter (d)) within the patch; Tanino and Nepf based their calculations on the average velocity within the patch. The drag coefficient, C_D, can be affected by the root density, the root Reynolds number, and the morphology of the individual canopy elements [7,15]. For a random arrangement, which is used by Tinoco and Cowen [39] and Chen *et al.* [32], the flow obstruction is more significant, which reduces the mean velocity value within the patch and consequently, the velocity difference between the upstream and downstream regions of the patch increases. Therefore, based on Tanino and Nepf [7], the drag coefficient is greater when using a random arrangement as compared to our case.

For all cases, we used an aligned arrangement, which is expected to facilitate the flow through the physical model. This effect is expected to be stronger in the most porous patch. For the aligned arrangement, the vortex street of the individual roots within the patch is formed [40]. Thus, the arrangement of the cylinders within the patch causes them to function as uncoupled cylinders, and most likely individual cylinder wakes are generated. As a result, the flow can pass between the individual roots at a greater velocity and the bleed flow from the patch increases. The bleed flow not only decreases the drag coefficient, but also delays the interaction of the shear layers and formation of the von Kármán vortex street. The effective diameter can be interpreted as the "obstruction seen" by the flow. Therefore, any change in cylinder arrangement that leads to a change in drag will also result in a change in the flow structure. The change in flow structure will cause a change in the effective diameter.

Figures 8(d)–8(f) shows the blockage parameter ($C_D a D$) as a function of energy release per vortex cycle, $\frac{C_D}{\text{St}}$, using patch diameter, equivalent length, and effective diameter as the length scale. The blockage is a nondimensional parameter that describes the resistance of the fluid to flow through the physical model. In this parameter, the effects of porosity and cylinder arrangement are taken into

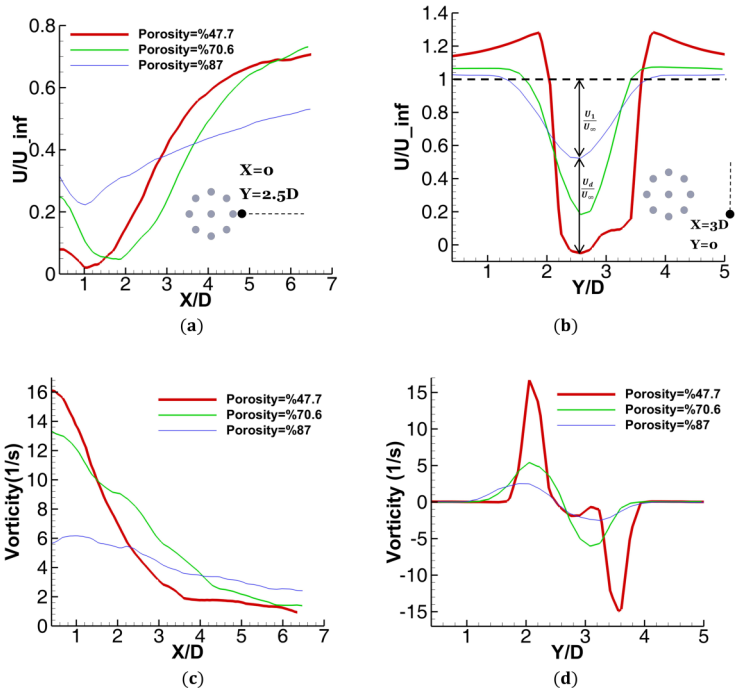

FIG. 9. Longitudinal (a) and cross-sectional (b) time-averaged x-velocity profiles for cases 1–3. Longitudinal (c) and cross-sectional (d) time-averaged z-vorticity profiles for cases 1–3. Panels show the comparison between different porosities. The vorticity magnitude decays with porosity increase. Dotted lines represent the line of measurement with the line origin (dark dot).

account through the drag coefficient. Low values of the blockage parameter could be due to high porosity (i.e., low solidity resulting in the fluid flowing easily through the physical model) or aligned arrangement of the cylinders, thus facilitating the fluid flow through the model. For example, for cases 1–3, as the arrangement was not modified, the blockage parameter increases as the porosity decreases.

The drag coefficient specifies the amount of energy that is absorbed by the patch per unit time. Based on conservation of momentum, the absorbed energy equals the energy released in the wake. Similarly, the Strouhal number indicates a nondimensional frequency of vortex shedding in a period of vortex shedding. Therefore, $\frac{C_D}{\mathrm{St}}$ is the ratio of energy released in the fluid for one period of the vortex shedding. Figures 8(d)–8(e) show that the energy released in the wake increases monotonically as patch blockage grows. Furthermore, independent of the length scale used, the blockage parameter versus energy release per vortex follows a linear relationship. As expected, there is a greater amount of energy release as the blockage parameter increases. The linear change of blockage parameter with respect to energy release implies that the ratio of $\frac{C_D a D}{\frac{C_D}{\mathrm{St}}}$ is almost constant for different porosities; therefore, $\mathrm{St} a D$ is a nondimensional parameter in the flow that describes the hydrodynamics of mangrove root-type models.

Time-averaged velocities were used to reveal the flow structure characteristics and provide insight into the effect of the flow structure on hydrodynamic forces acting on the entire patch. The variations of time-averaged streamwise velocity nondimensionalized by upstream velocity are shown in Fig. 9. Figure 9(a) shows that with an increase in porosity, minimum streamwise velocity increases in the near wake, and the minimum velocity shifts to the greater values (from $\frac{U}{U_\infty} = 0.25$ to 2.25). The narrow wake structure in the spanwise direction on the cylinder results in a reduced drag force as depicted in Fig. 4(a). As a result, the patch drag force decreases approximately 30% and 10% for

$\varphi = 70\%$ and $= 86\%$ from the drag force of $\varphi = 47\%$, respectively. Consequently, the wake length, L_1, elongates (Fig. 7) and delays the formation of von Kármán vortex street consistent with Chen *et al.* [32]. Thus, the wake width narrows considerably with porosity [Figs. 5(a)–5(c)], postponing the decay of shear layers and shifting the location of minimum wake velocity to greater values [Fig. 9(a)].

The streamwise velocity decreases to its minimum value and then increases toward the value of the upstream velocity farther downstream of the patch. The velocity leaving the shear layer boundary ($0.5 < \frac{Y}{D} < 1.5$ and $4 < \frac{Y}{D} < 5$) is similar to the upstream velocity for $\varphi = 87\%$ [Fig. 9(b)]. The velocity slightly changes with porosity, which is most likely due to the wall effect for a closed water tunnel. The wall effect may slightly confine the boundaries; however, in our experiments, the ratio of patch diameter to water channel width is 0.1 and the confinement does not suppress the formation of von Kármán vortex street. There is evidence of reverse flow ($\frac{U}{U_\infty} < 0$) at $\frac{Y}{D} = 2.5$ for $\varphi = 47\%$, which indicates that streamwise velocity decreases toward the center of the wake and is minimum at $\frac{Y}{D} = 2.5$, where strong interactions of the shear layers and vortical structure initiates. The minimum value of $\frac{U}{U_\infty}$ for all porosities occurs at $\frac{Y}{D} = 2.5$ and increases with porosity. However, the reverse flow is not observed for greater porosities.

Figure 9(c) shows the vorticity magnitude calculated along the mid-line for three patches with different porosities. The vorticity magnitude just downstream of the physical models increases as the porosity decreases (larger blockage). However, the rate at which the vorticity decreases along the downstream direction is greater for lower porosity. Therefore, the downstream distance needed for the vorticity magnitude to decay is shorter for lower porosity even though it has a greater vorticity value closer to the patch.

Figure 9(d) shows the vorticity in the transverse direction. The velocity along this axis exhibits a positive and negative peak at $\frac{Y}{D} = 2$ and $\frac{Y}{D} = 3.5$, respectively, and the vorticity peaks diminish as porosity increases. There is a sharp vorticity magnitude reduction ($\Delta\omega = 15\ \frac{1}{s}$) in the vicinity of $\frac{Y}{D} = 2$ and $\frac{Y}{D} = 3.5$ for the dense patch ($\varphi = 47\%$). The reduction in the vorticity magnitude for the porous patch ($\varphi = 87\%$) is approximately one-third ($\Delta\omega = 5\ \frac{1}{s}$) of the dense patch.

By applying the conservation of momentum to a control volume downstream of the patch and neglecting the viscous forces, the mean drag force on the entire patch can be derived from the velocity and pressure in a plane in the wake of the patches as

$$F_D = h\rho \int_{-\infty}^{+\infty} u_1(U_\infty - u_1)\, dy + \int_{-\infty}^{+\infty} (P_\infty - P_1)\, dy, \tag{19}$$

where F_D is the drag force, ρ is the water density, h is the height of the body, and u_1 and p_1 are the velocity and pressure in the wake at point y, respectively.

The pressure term is expected to vanish at a sufficiently large distance from the cylinder, while the momentum term reaches an asymptotic value [41]. As reported by Terra *et al.* [42], for rough cylinders, the pressure term rapidly decays after $\frac{X}{D} = 1.5$ and remains fluctuating around zero. Therefore, by assuming that flow process without losses (i.e., the total pressure remains constant along the streamlines), the pressure terms can be neglected and the drag on the entire patch can be estimated by measuring the velocity distribution in the wake [43]. As is shown in Fig. 9(b), the velocity in the wake (u_1) is smaller than the uniform upstream velocity (u_∞) which generates velocity deficit in the wake ($U_d = U_\infty - u_1$). This velocity deficit is associated with the drag acting on the entire patch.

The drag coefficient estimated through PIV measurement is compared with drag coefficient based on patch diameter [Eq. (6)] obtained by direct force measurement and the empirical curve fit based on the effective diameter as the length scale [Eq. (15)]. The drag coefficient based on direct measurement and the estimated values through PIV are seen to follow a similar decreasing trend with porosity (Fig. 10).

Figure 10 shows that the drag coefficient decreases with porosity. This is mainly due to the wake behind the highly porous patch being narrower and the momentum deficit considerably lower, compared to the dense patch, indicating a lower drag for the former. The highly porous patch reveals a

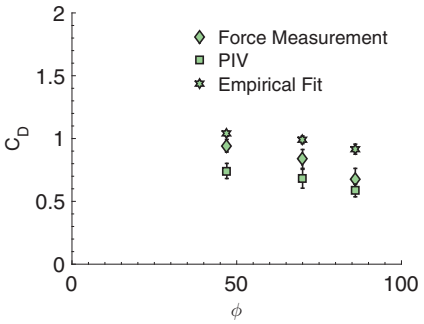

FIG. 10. Drag coefficient with respect to porosity based on force measurement (diamond), flow measurements (square) and empirical fit from Eq. (19) (star). Vertical bar shows 95% confidence interval. The values are for $\mathrm{Re}_D = 3000$ and cases 1–3. Vertical bar shows 95% confidence interval.

weak shear layer interaction and decreased velocity gradient in the wake when compared to the dense patch [Figs. 5(d)–5(f)]. Therefore, less velocity fluctuation and a smaller wake behind the highest porous patch were observed. Consequently, the drag force is dramatically reduced (Fig. 10). [Note the substantial difference in the size of the wake for the porous patch flow shown in Figs. 5(j)–5(l) compared with the dense patch.] The reduced wake leads to a significant reduction in the drag. This is mainly because flow energy is spent on energizing the boundary layer separation, shear layer eddy mixing, and reattaching the flow to the patch. Therefore, the fluid energy is diminished by porosity which results in a narrow wake formation and drag reduction (Fig. 10). This can also be corroborated by the weakening Reynolds stress, which is associated with a reduction in momentum flux with porosity in the wake [Figs. 5(g)–5(i)].

Figure 10 shows that the drag coefficient can be estimated based on flow field measurement sufficiently downstream from the patch. The difference between PIV and direct force measurement could be attributed to the neglected pressure terms [Eq. (19)] generated by the patch that distort the flow streamlines and contribute to the underestimation of the drag coefficient. A relatively intense turbulence level (max 60%), small three-dimensional effects in the flow due to the open channel section, and presence of the wall effect (about 0.1) are possible sources of difference between force measurements and drag derivation through PIV.

Figure 10 shows that the drag coefficient based on effective diameter length scale follows the same trend with porosity, although it is greater than the drag coefficient based on the patch diameter. This can be partly explained by a reduction in the magnitude of the effective diameter, which ranged from $0.45 < \frac{D_{\mathrm{eff}}}{D} < 0.8$ [Fig. 4(b)]; therefore, with the same drag force, the drag coefficient reaches greater values compared to patch length scale D. For the least porous patch ($\varphi = 47\%$), the difference in drag coefficient based on patch and effective diameter length scales is insignificant ($\sim$5%) since both length scales have similar values ($\frac{D_{\mathrm{eff}}}{D} = 0.8$). Additionally, the difference in drag coefficient based on patch and effective diameter length scales is due to the fact that effective diameter incorporates the variation of spacing ratio and the cylinder arrangement within the patch, which is not included in a drag coefficient based on the patch diameter.

VII. CONCLUSION

We studied the hydrodynamics of mangrove roots using circular arrays of cylinders as a simplified model. We conducted direct force measurement and PIV flow measurements in a recirculating flume as a function of porosity and flow speed. We found that the Strouhal number increases with porosity but the Strouhal number was almost constant with Reynolds number. The Strouhal number for the highest porosity was more than twice that of a solid cylinder. We introduced a length scale—the effective diameter (D_{eff})—that can be used to relate the wake signature of a model to the Strouhal

number of a solid cylinder. This length scale is the effective solid diameter "experienced" by the flow. We compared the drag coefficients of the physical model that were generated using three different length scales: the patch of cylinders based on patch diameter *(D)*, the equivalent length (L_E) introduced by Mazda *et al.*, and the effective diameter (D_{eff}). We found that the effective diameter was an appropriate length scale to collapse in a common curve the drag coefficient, thus reflecting the effect of porosity, diameter of the cylinders, and the patch diameter. We also found that the blockage, $C_D a D$, of the physical model has a linear relationship with the energy released. Based on that, we defined StaD as a nondimensional constant that describes the hydrodynamics of mangrove root-type models.

Regarding the flow measurements, we found that the mean of the flow parameters, including velocity deficit, vorticity, Reynolds shear stresses, and turbulence behind the patch, decreased with porosity. However, the length of the wake tended to increase with porosity. The time-resolved PIV measurements showed that the flow structure impacted the drag coefficient by changes in the velocity deficit and subsequent changes in dispersive terms.

The proposed effective diameter length scale appears to be suitable to estimate the drag coefficient of a porous patch of cylinders. Although our models were based on the structure of an isolated patch of mangrove roots, our results could have implications for investigations of other fluid challenges, including flow through either porous objects, vegetation, or an array of objects. An understanding of the hydrodynamics and scaling of this problem could also contribute to the design and development of a bio-inspired mangrove-like system for coastal protection.

ACKNOWLEDGMENTS

The authors are grateful for support for this project, which was generously provided by a Link Foundation Ocean Engineering and Instrumentation Ph.D. Fellowship Program (Award No. AWD-001009). This work was also partially supported by a FAU seed grant to O.M.C. and K.V.D.R.

[1] S. Quartel, A. Kroon, P. G. E. F. Augustinus, P. Van Santen, and N. H. Tri, Wave attenuation in coastal mangroves in the Red River Delta, Vietnam, J. Asian Earth Sci. **29**, 576 (2007).

[2] K. Kim, E. Seo, S.-K. Chang, T. J. Park, and S. J. Lee, Novel water filtration of saline water in the outermost layer of mangrove roots, Sci. Rep. **6**, 20426 (2016).

[3] K. B. Gedan, M. L. Kirwan, E. Wolanski, E. B. Barbier, and B. R. Silliman, The present and future role of coastal wetland vegetation in protecting shorelines: Answering recent challenges to the paradigm, Clim. Change **106**, 7 (2011).

[4] K. Kathiresan and B. L. Bingham, Biology of mangroves and mangrove ecosystems, Adv. Mar. Biol. **40**, 81 (2001).

[5] I. Nagelkerken, A. M. De Schryver, M. C. Verweij, F. Dahdouh-Guebas, G. van der Velde, and N. Koedam, Differences in root architecture influence attraction of fishes to mangroves: A field experiment mimicking roots of different length, orientation, and complexity, J. Exp. Mar. Biol. Ecol. **396**, 27 (2010).

[6] T. J. Bouma, L. A. van Duren, S. Temmerman, T. Claverie,A. Blanco-Garcia, T. Ysebaert, and P. M. J. Herman, Spatial flow and sedimentation patterns within patches of epibenthic structures: Combining field, flume and modelling experiments, Cont. Shelf Res. **27**, 1020 (2007).

[7] K. Furukawa, E. Wolanski, and H. Mueller, Currents and sediment transport in mangrove forests, Estuarine, Coastal Shelf Sci. **44**, 301 (1997).

[8] Y. Mazda, M. Magi, M. Kogo, and P. N. Hong, Mangroves as coastal protection from waves in the Tong King delta, Vietnam, Mangroves Salt Marshes **1**, 127 (1997).

[9] S. Das and J. R. Vincent, Mangroves protected villages and reduced death toll during Indian super cyclone, Proc. Natl. Acad. Sci. USA **106**, 7357 (2009).

[10] A. Strusińska-Correia, S. Husrin, and H. Oumeraci, Sunami damping by mangrove forest: A laboratory study using parameterized trees, J. Natural Hazards Earth Sys. Sci. **13**, 483 (2013).

[11] Y. Mazda, N. Kanazawa, and E. Wolanski, Tidal asymmetry in mangrove creeks, Hydrobiologia **295**, 51 (1995).
[12] A. Kazemi and O. Curet, PIV measurements and flow characteristics downstream of mangrove root models, APS Division of Fluid Dynamics, Portland, Fall 2016, abstract D3.005 (2016).
[13] D. M. Alongi, Mangrove forests: Resilience, protection from tsunamis, and responses to global climate change, Estuarine, Coastal Shelf Sci. **76**, 1 (2008).
[14] E. M. Horstman, C. M. Dohmen-Janssen, and S. J. M. H. Hulscher, Flow routing in mangrove forests: A field study in Trang province, Cont. Shelf Res. **71**, 52 (2013).
[15] E. Wolanski, Hydrodynamics of mangrove swamps and their coastal waters, Hydrobiologia **247**, 141 (1992).
[16] K. Kathiresan, How do mangrove forests induce sedimentation? Rev. Biol. Trop. **51**, 355 (2003).
[17] R. Chen and R. R. Twilley, Patterns of mangrove forest structure and soil nutrient dynamics along the Shark River Estuary, Florida, Estuaries **22**, 955 (1999).
[18] T. J. Smith, G. H. Anderson, K. Balentine, G. Tiling, G. A. Ward, and K. R. T. Whelan, Cumulative impacts of hurricanes on Florida mangrove ecosystems: Sediment deposition, storm surges and vegetation, Wetlands **29**, 24 (2009).
[19] K. W. Krauss, T. J. Doyle, T. W. Doyle, C. M. Swarzenski, A. S. From, R. H. Day, and W. H. Conner, Water level observations in mangrove swamps during two hurricanes in Florida, Wetlands **29**, 142 (2009).
[20] E. Wolmski, M. Jones, and J. S. Bunt, Hydrodynamics of a tidal creek-mangrove swamp system, Mar. Freshwater Res. **31**, 431 (1980).
[21] W. Vandenbruwaene, T. Maris, T. J. S Cox, D. R. Cahoon, P. Meire, and S. Temmerman, Sedimentation and response to sea-level rise of a restored marsh with reduced tidal exchange: Comparison with a natural tidal marsh, Geomorphology **130**, 115 (2011).
[22] J. C. Mullarney, S. M. Henderson, J. A. H. Reyns, B. K. Norris, and K. R. Bryan, Spatially varying drag within a wave-exposed mangrove forest and on the adjacent tidal flat, Cont. Shelf Res. **147**, 102 (2017).
[23] Y. Mazda, E. Wolanski, B. King, A. Sase, D. Ohtsuka, and M. Magi, Drag force due to vegetation in mangrove swamps, Mangroves Salt Marshes **1**, 193 (1997).
[24] R. O. Tinoco and G. Coco, Observations of the effect of emergent vegetation on sediment resuspension under unidirectional currents and waves, Earth Surface Dyn. **2**, 83 (2014).
[25] B. K. Norris, J. C. Mullarney, K. R. Bryan, and S. M. Henderson, The effect of pneumatophore density on turbulence: A field study in a Sonneratia-dominated mangrove forest, Vietnam, Cont. Shelf Res. **147**, 114 (2017).
[26] T. Takemura and N. Tanaka, Flow structures and drag characteristics of a colony-type emergent roughness model mounted on a flat plate in uniform flow, Fluid Dyn. Res. **39**, 694 (2007).
[27] Y. Wu, R. A. Falconer, and J. Struve, Mathematical modelling of tidal currents in mangrove forests, Env. Model. Softw. **16**, 19 (2001).
[28] Y. Mazda and E. Wolanski, Hydrodynamics and modeling of water flow in mangrove areas, in *Coastal Wetlands: An Integrated Ecosystem Approach* (Elsevier, Amsterdam, 2009), pp. 231–261.
[29] J. Struve, R. A. Falconer, and Y. Wu, Influence of model mangrove trees on the hydrodynamics in a flume, Estuarine, Coastal Shelf Sci. **58**, 163 (2003).
[30] S. Petryk, Drag on cylinders in open channel flow, Ph.D. thesis, Colorado State University, Fort Collins, Colorado, 1969.
[31] Y. H. N. Tanino, Laboratory investigation on mean drag in a random array of rigid, emergent cylinders, J. Hydraulic Eng. **134**, 34 (2008).
[32] Z. Chen, A. Ortiz, L. Zong, and H. Nepf, The wake structure behind a porous obstruction and its implications for deposition near a finite patch of emergent vegetation, Water Resour. Res. **48**, W09517 (2012).
[33] L. Zong and H. Nepf, Flow and deposition in and around a finite patch of vegetation, Geomorphology **116**, 363 (2010).
[34] L. Zong and H. Nepf, Vortex development behind a finite porous obstruction in a channel, J. Fluid Mech. **691**, 368 (2011).
[35] H. Nepf, Hydrodynamics of vegetated channels, J. Hydraulic Res. **50**, 262 (2012).

[36] A. C. Ortiz, A. Ashton, and H. Nepf, Mean and turbulent velocity fields near rigid and flexible plants and the implications for deposition, J. Geophys. Res. Earth Surf. **118**, 2585 (2013).
[37] A. Kazemi, K. Van de Riet, and O. M. Curet, Hydrodynamics of mangrove-type root models: The effect of porosity, spacing ratio and flexibility, Bioinspir. Biomim. **12**, 056003 (2017).
[38] F. M. White, *Viscous Fluid Flow* (McGraw-Hill, New York, 1991).
[39] R. O. Tinoco and E. A. Cowen, The direct and indirect measurement of boundary stress and drag on individual and complex arrays of elements, Exp. Fluids **54**, 1509 (2013).
[40] A. Nicolle and I. Eames, Numerical study of flow through and around a circular array of cylinders, J. Fluid Mech. **679**, 1 (2011).
[41] J. D. Anderson, *Fundamentals of Aerodynamics* (McGraw-Hill, New York, 2011).
[42] W. Terra, A. Sciacchitano, and F. Scarano, Drag analysis from PIV data in speed sports, Procedia Eng. **147**, 50 (2016).
[43] H. Schlichting, *Boundary-Layer Theory*, 7th ed. (McGraw-Hill, New York, 1979), Vol. 1, p. 274.